processes

MDPI

Article

Reliability of Different Nanofluids and Different Micro-Channel Configurations on the Heat Transfer Augmentation

Ibrahim Elbadawy *, Abdulaziz Alhajri, Mohammad Doust, Yousef Almulla, Mohamed Fayed, Ali Dinc, Mohamed Abouelela, Ibrahim Mahariq and Wael Al-Kouz *

College of Engineering and Technology, American University of the Middle East, Kuwait
* Correspondence: ibrahim.mohamed@aum.edu.kw (I.E.); wael.kouz@aum.edu.kw (W.A.-K.)

Abstract: Nanofluid, the fluid suspensions of a metallic nanoparticle, became a coolant fluid that is used when a promising enhancement in heat transfer is required. In the current study, the characteristics of fluid flow and heat transfer are numerically investigated using different nanofluids (Al_2O_3–H_2O, TiO_2–H_2O, and SiO_2–H_2O) and different micro-channel heat sink (MCHS) configurations (rectangular, triangular, trapezoidal, and circular). In this numerical investigation, the effect of Re number ranged from 890 to 1500, and the effect of nanoparticle concentration ranged from 1% to 7% at constant heat flux q = 10^6 W/m^2, and constant fluid inlet temperature of 288 K, were studied. The average heat transfer coefficient, h, and pressure drop, Δp, are used to quantify the fluid flow and heat transfer characteristics in each MCHS configuration and for each nanoparticle concentration. It is revealed that a better heat transfer coefficient is obtained for Al_2O–H_2O compared with other types of nanoparticles and pure water, such as 8.58% heat transfer coefficient improvement obtained at Re = 1500 and φ = 7% more than that of pure water. It is also inferred that the maximum heat transfer coefficient is obtained by the triangular MCHS; however, it has the highest pressure drop because of the lowest hydraulic diameter.

Keywords: CFD; nanofluids; microchannels; MCHS configurations

Citation: Elbadawy, I.; Alhajri, A.; Doust, M.; Almulla, Y.; Fayed, M.; Dinc, A.; Abouelela, M.; Mahariq, I.; Al-Kouz, W. Reliability of Different Nanofluids and Different Micro-Channel Configurations on the Heat Transfer Augmentation. *Processes* **2023**, *11*, 652. https://doi.org/10.3390/pr11030652

Academic Editor: Alfredo Iranzo

Received: 30 January 2023
Revised: 13 February 2023
Accepted: 20 February 2023
Published: 21 February 2023

1. Introduction

With the rapid advancement of nano-technologies, the number of chips used in devices is continuously increasing and leading to high circuit complexity. This increases the requirement of heat dissipation in a very small area of electronic devices such as processors. That leads to an overheating problem which is one of the main reasons for electronic chip damage. As a result, using liquid (water), air, and hybrid air-water cooling systems become necessary. However, these types of cooling systems are not effective in the cooling process due to rapid more in technology development. In addition, it is necessary to explore an alternative and effective method rather than conventional ones to remove a significant amount of heat transfer. Tuckerman and Pease [1], in 1981, first proposed the MCHS, which is one of the most convenient methods for effective cooling electronic devices. In the very beginning, pure water in a single phase is used as a coolant, and a significant heat transfer enhancement was achieved. For instance, the generated heat flux reaching 790 W/cm^2 is dissipated. Additionally, it is reported that decreasing the width of the microchannel leads to improving convective heat transfer. On the contrary, due to more technological improvements, the usage of pure water as a coolant in MCHS has not become effective. Therefore, it is important to find alternative ways to improve heat transfer dissipation that can compete with quick technology improvements.

The most common channel is the straight rectangular MCHS, which is inadequate to absorb the total heat generated by micro-scale chip devices. Therefore, Chen et al. [2] studied numerically different configurations of microchannels, such as the rectangular,

trapezoidal, and triangular microchannels, and their effect on heat transfer characteristics. The average Nusselt number, Poiseuille number, temperature, and thermal efficiency are the key parameters of this study. It is revealed that the Nusselt number has the highest value at the microchannel inlet and then significantly decreases to be a fully developed constant value for all configurations, while the triangular shape achieves the maximum thermal efficiency (thermal efficiency: heat transfer rate to the rate of power consumption) among the three configurations. The effect of different microchannel configurations on heat transfer characteristics and laminar flow was numerically investigated for a low range of Reynolds numbers from 100–1000 by Gunnasegaran et al. [3]. Rectangular, trapezoidal, and triangular are the main shapes in this study. It is found that at the smallest hydraulic diameter, better uniformities in the temperature and heat transfer coefficient can be achieved. Additionally, the smallest hydraulic diameter offers lower pressure drop as well as power consumption. The highest heat transfer coefficient and Poiseuille number are achieved for a rectangular microchannel, while the lowest values are for the triangular configuration. The pressure drop is studied at different heat fluxes of 100, 500, and 1000 W/m^2, and it is found that increasing heat flux leads to increased pressure drop.

A 3-D numerical simulation of laminar water flow through a grooved microchannel aluminum heat sink is studied by Ahmed and Ahmed [4]. A constant wall heat flux forced convection heat transfer, and different cavity shapes (rectangular, triangular, and trapezoidal) are used as key parameters under investigation. It is found that a trapezoidal groove with a groove pitch ratio of 3.334, tip length ratio of 0.5, and groove depth ratio of 0.4 gives a significant improvement in flow and heat transfer characteristics. For example, Nusselt number improvement is 51.59% while the friction factor enhancement is 2.35%.

On the other hand, the thermal conductivity of the coolant is a crucial parameter that affects the improvement of the heat transfer characteristics [5]. Choi and Eastman [6] explored a new type of coolant that is called nanofluid, which can be formed by mixing nanoparticles of metallic substance with traditional heat transfer base fluids, such as pure water. This mixture produces nanofluids with new and good thermal properties (such as thermal conductivity) compared with those of base fluids. Godson et al. [7] reported that the increase of nanofluid thermal conductivity leads to significant enhancement of the cooling process. In addition, Tokit et al. [8] mentioned that the Brownian motion, which plays a vital role in helping the nanoparticle cluster formation, is considered the main reason for high thermal conductivity. In addition, Das et al. [9] showed that using CuO-H_2O leads to an increase the thermal conductivity from 14% to 36%, which causes a significant effect on heat transfer characteristics.

Salman et al. [10] studied the effect of mixing different types of nanoparticles (CuO, Al_2O_3, ZnO, and SiO_2) mixed with ethylene glycol as a base fluid at different volume concentrations, sizes, and Reynolds numbers. Salman et al. reported that increasing the volume fraction of nanoparticles leads to improvement in the cooling process while increasing the nanoparticle diameters inversely affects the heat transfer for all cases. Additionally, Nguyen et al. [11] found that using a 6.8% volume fraction of Al_2O_3–H_2O nanofluid leads to an increase in the coefficient of heat transfer by 40% compared with base fluid (pure water). The same nanofluid of Nguyen et al.'s study is used by Elbadawy and Fayed [12] to study the effect of Al_2O_3–H_2O flow through single and double-stack MCHS. Constant heat flux ($q = 10^6$ W/m^2), laminar flow (Re = 200–1500), and different nanoparticle concentrations (φ = 1–5%) are the main parameters under investigation. Elbadawy and Fayed [12] evaluate how much volume reduction is obtained caused by the improvement in nanofluid thermal conductivity as well as the characteristics of heat transfer. It is reported that a 62.6% size reduction was achieved for a single channel row at a 5% nanoparticle concentration. Mohamed et al. [13] investigated the effect of different nanoparticles (Al_2O_3, diamond, TiO_2, SiO_2, Ag, and CuO) with base fluid (pure water) and triangular microchannel on fluid flow and heat transfer characteristics. Heat transfer coefficient, pressure drop, power, and thermal resistance are used as key parameters. Diamond-H_2O leads to the lowest temperature and highest heat transfer coefficient, while the highest and lowest pressure

drop occurred for SiO_2–H_2O and Ag–H_2O, respectively. Finally, it is worth mentioning that nanofluids and hybrid nanofluids have been investigated for different geometries along with the impact of different physical parameters; these include the porous media effect, rarefied flows, and magnetohydrodynamics [14–23].

Through an extensive survey of the literature, it is aimed that prior work related to the computational investigation of nanofluids, the heat transfer, and flow through MCHS using different nanofluids and different MCHS configurations are carefully and extensively investigated. Therefore, Al_2O_3–H_2O, SiO_2–H_2O, and TiO_2–H_2O and different MCHS configurations (rectangular, trapezoidal, triangular, and circular) are numerically investigated. In addition, the different volume fractions of nanoparticles (1% to 7%) and laminar flow (Re = 890 to 1500) are used. The heat transfer coefficient, pressure drop along the channel, and thermal efficiency are used as key parameters using the CFD software (ANSYS-Fluent 18.2) [24].

2. Mathematical Modeling

The constant heat flux applied to the heat sink base can be eradicated using MCHS by flowing different nanofluids as coolant with water as base fluid. Figures 1–4 illustrate the different MCHS configurations that are used in the current investigation. All dimensions for all configurations are listed in Table 1. For numerical solution purposes, a finite volume technique is employed. The governing equations are discretized utilizing a second-order hybrid accuracy scheme of upwind and central differences to differentiate the convective terms. A mesh of cell volumes 20 μm^3 is used for all simulations after performing a grid independency test. The pressure field is evaluated based on the PRESTO algorithm by implementing the SIMPLE algorithm adopted from [24]. The solution converges at the point where the maximum normalized absolute residual over all nodes is under 10^{-6}.

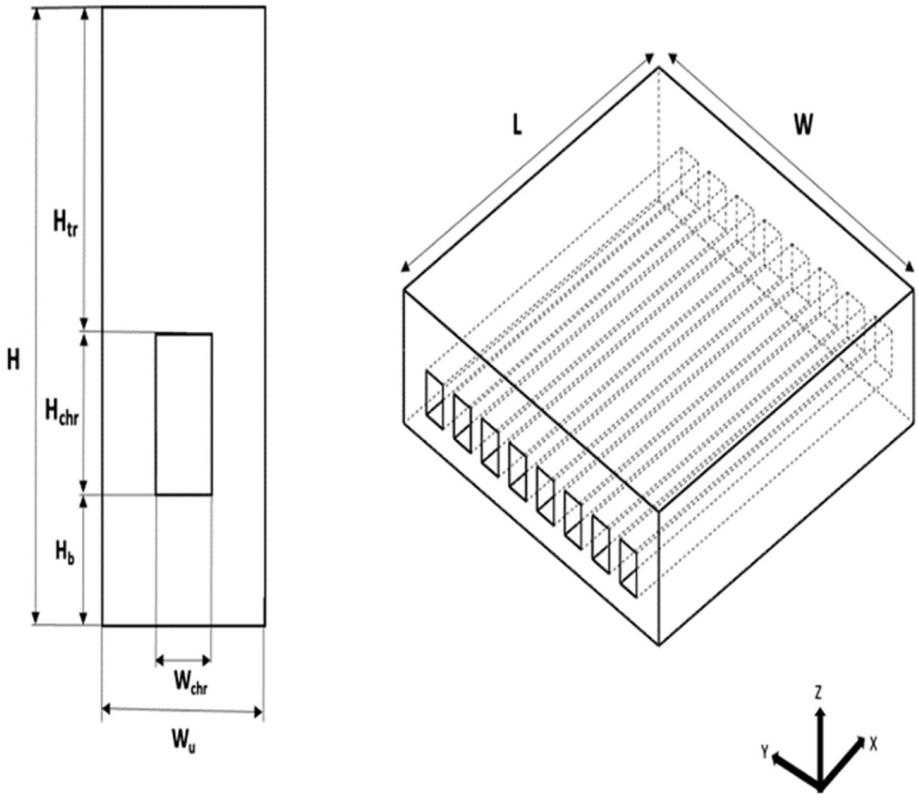

Figure 1. Rectangular MCHS.

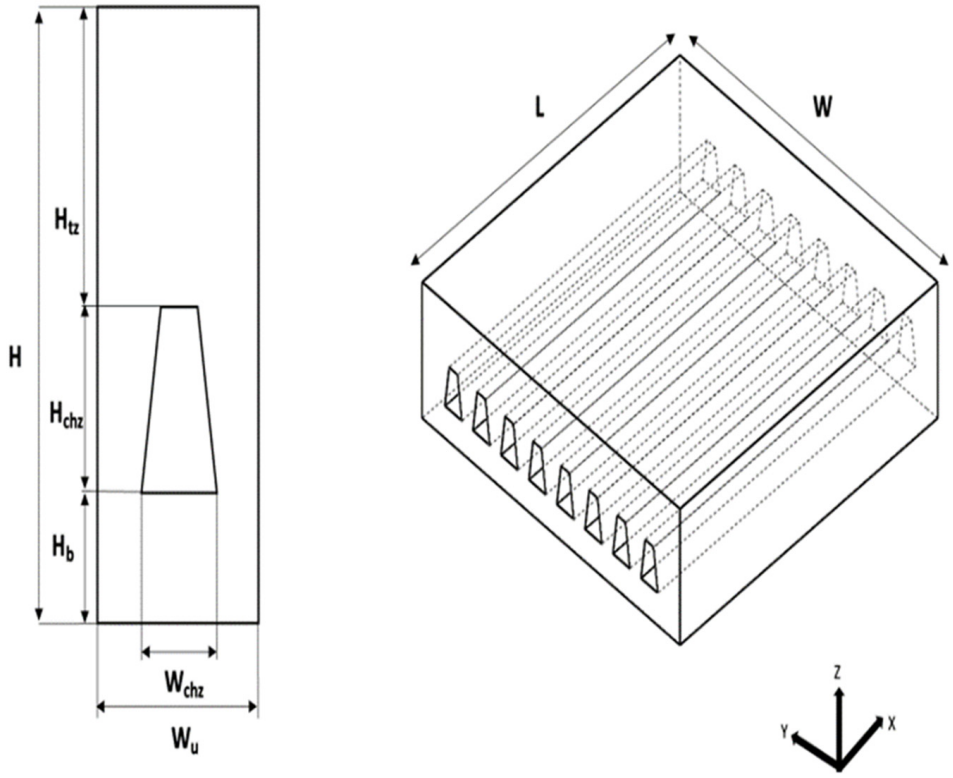

Figure 2. Trapezoidal MCHS.

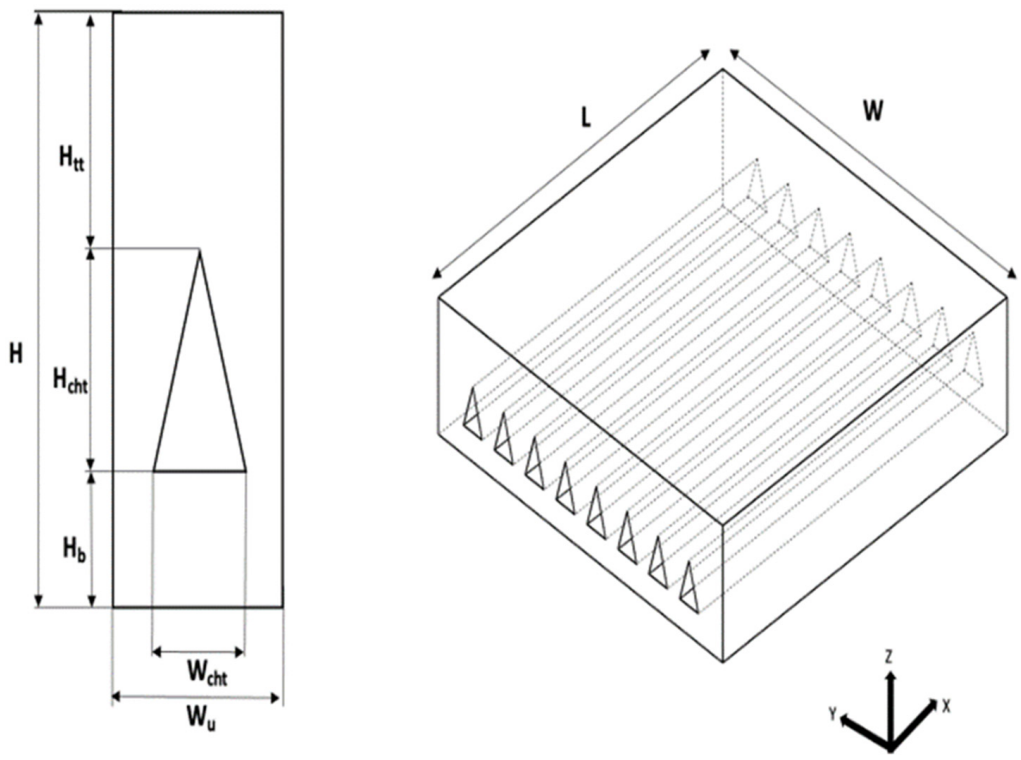

Figure 3. Triangle MCHS.

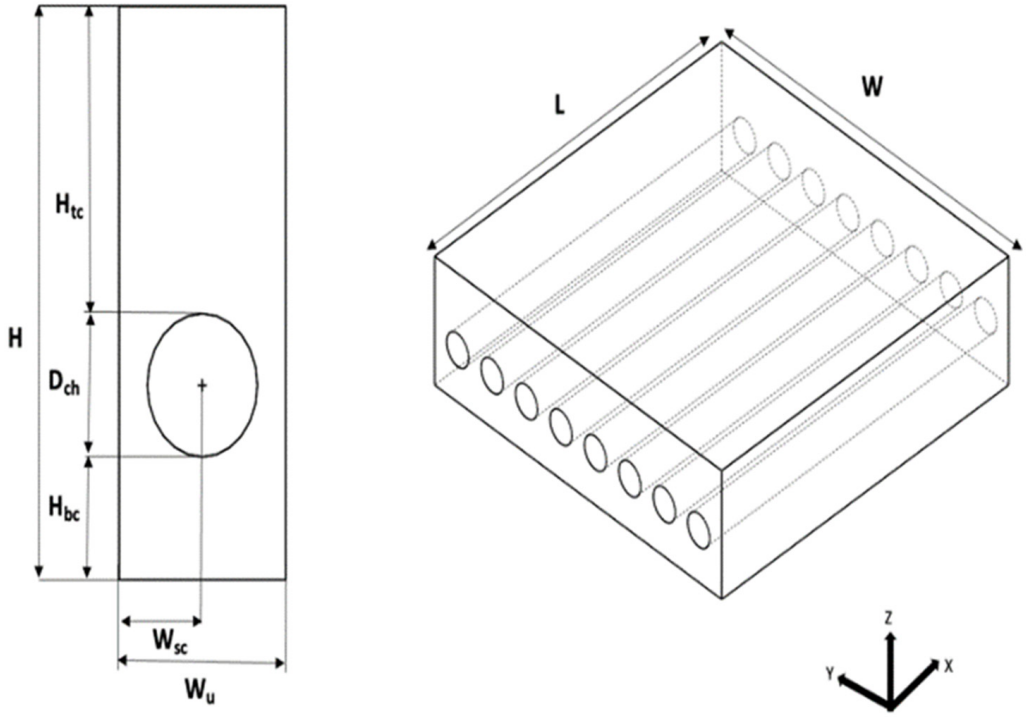

Figure 4. Circular MCHS.

Table 1. MCHS' Dimensions for the different configurations.

Parameters	Values [mm]
W_{ch}: width of the channel	0.231
H_{ch}: height of the channel	0.713
L: length of the channel	44.764
W_u: width of the unit	0.467
H: height of the unit cell	19.05
H_t: rectangular microchannel tip thickness	13.700
H_{tz}: trapezoidal microchannel tip thickness	13.46233
H_{tt}: triangular microchannel tip thickness	12.987
H_{tc}: circular microchannel tip thickness	13.955
H_B: distance from the channel bottom wall to the base of the unit cell	4.637
H_{th}: thermocouple location	3.175

2.1. Governing Equations

The conservation of mass, momentum, and energy governing equations [25] were solved based on the assumptions illustrated in Table 2.

Table 2. Assumption [26].

Parameters	Assumptions
Flow characteristics	Three-dimensional, steady, laminar, incompressible, and single phase
Body force	Neglected
Heat transfer by radiation	Neglected
Slip condition	No slip, $u = v = w = 0$ at the solid wall [27,28]
Inlet velocity	Uniform [27,28]
Number of microchannels	One channel is investigated due to the similarity of flow and heat transfer [29]

Continuity:

$$\nabla.\mathbf{V} = 0, \tag{1}$$

where **V** is the flow vector of velocity (m/s).

Momentum:

$$\rho_{nf}(\nabla.\mathbf{V})\mathbf{V} = -\nabla P + \mu_{nf}\nabla^2\mathbf{V}\,, \tag{2}$$

where the nanofluid density is ρ_{nf} (kg/m^3), the pressure is P (Pa), and the nanofluid dynamic viscosity is μ_{nf} (kg/m.s).

Energy:

$$\rho_{nf}C_{p_{nf}}(\nabla.\mathbf{V})T = k_{nf}\nabla^2 T\,, \tag{3}$$

where the specific heat of the nanofluid is $C_{p_{nf}}$ (J/kg·k), the nanofluid thermal conductivity is k_{nf} (W/m·k), and the flow temperature is T (K).

2.2. Thermophysical Properties of Nanofluids:

Because of the small changes in fluid temperature along the channel, the constant thermophysical properties can be considered for nanofluids at different volume concentrations. In the current study, pure water (base fluid) mixed with the solid particles (Al_2O_3, TiO_2, and SiO_2) at different volume concentrations are used to form different nanofluids with different thermophysical properties. The new properties can be calculated by the correlations listed below [30].

Thermal conductivity [W/m·k]:

$$k_{nf} = \left[\frac{k_p + (n-1)k_{bf} - (n-1)\varphi\left(k_{bf} - k_p\right)}{k_p + (n-1)k_{bf} + \varphi\left(k_{bf} - k_p\right)}\right]k_{bf}, \tag{4}$$

where the solid particle shape factor is n = 3 for particles in a spherical shape assumption.

Dynamic viscosity [kg/m·s]:

$$\frac{\mu_{nf}}{\mu_{bf}} = 1 + 2.5\varphi. \tag{5}$$

Density [kg/m^3]:

$$\rho_{nf} = (1-\varphi)\rho_{bf} + \varphi\rho_p. \tag{6}$$

Heat capacity [J/kg·k]:

$$c_{p_{nf}} = (1-\varphi)c_{p_{bf}} + \varphi c_{p_p}, \tag{7}$$

where φ characterizes the particle volume fraction and the subscript "bf, nf, and p" are base fluid, nanofluids, and particle, respectively. Tables 3–5 illustrate the new thermophysical properties at different nanoparticles concertation for Al_2O_3, SiO_2, and TiO_2 at T = 288 K.

Table 3. Properties of Al_2O_3–H_2O [31].

Properties	**Nanoparticle (Al_2O_3)**	**Base Fluid (H_2O)**	**Nanofluid (Al_2O_3–H_2O)**				
			φ = 0.01	**0.03**	**0.05**	**0.06**	**0.07**
ρ	3970	997	1026.73	1086.19	1145.65	1175.38	1205.11
c_p	765	4185	4150.8	4082.4	4014	3979.8	3945.6
κ	36	0.613	0.63064929	0.66698407	0.70476938	0.7242334	0.74409385
μ		0.000855	0.00087638	0.00091913	0.00096188	0.00098325	0.00100463

Table 4. Properties of SiO_2–H_2O [32].

Properties	Nanoparticle (SiO_2)	Base Fluid (H_2O)	Nanofluid (SiO_2–H_2O)				
			Φ =0.01	**0.03**	**0.05**	**0.06**	**0.07**
ρ	2200	997	1009.03	1033.09	1057.15	1069.18	1081.21
c_p	740	4185	4150.55	4081.65	4012.75	3978.3	3943.85
κ	1.38	0.613	0.61842854	0.62938233	0.640467	0.64605916	0.65168492
μ		0.000855	0.00087638	0.00091913	0.00096188	0.00098325	0.00100463

Table 5. Properties of TiO_2–H_2O [31].

Properties	Nanoparticle (TiO_2)	Base Fluid (H_2O)	Nanofluid (TiO_2–H_2O)				
			Φ =0.01	**0.03**	**0.05**	**0.06**	**0.07**
ρ	4157	997	1028.6	1091.8	1155	1186.6	1218.2
c_p	710	4185	4150.25	4080.75	4011.25	3976.5	3941.75
κ	8.4	0.613	0.62799801	0.65874009	0.69051887	0.70681354	0.72338767
μ		0.000855	0.00087638	0.00091913	0.00096188	0.00098325	0.00100463

2.3. Numerical Data Calculations

The average heat transfer coefficient is "h".

Newton's cooling law, Equation (8), is used to calculate the total heat transfer rate.

$$Q = hA_s\Delta T = hA_s(T_b - T_s), \tag{8}$$

where the total microchannel surface area is A_s, the average fluid bulk temperature is T_b (Equation (9)), and the average microchannel temperature, T_s, is computed from the computation post-processing.

$$T_b = \frac{T_{in} + T_{out}}{2}, \tag{9}$$

where inlet and outlet fluid temperatures are T_{in} and T_{out}, respectively.

Then, from Equations (9) and (10), the average heat transfer coefficient can be determined as follows

$$h = \frac{q}{A_s(T_b - T_s)}. \tag{10}$$

Also, the average Nusselt number can be determined by:

$$Nu = \frac{hD_h}{k}, \tag{11}$$

where the hydraulic diameter, D_h, can be found by

$$D_h = \frac{4A}{p}, \tag{12}$$

where the channel cross-sectional flow area is A with wetted perimeter, p.

2.4. Parameters and Conditions

Different parameters, listed in Table 6, have been changed during this study to know the optimum values of these parameters that achieve high performance of heat transfer and lower pressure drop. Temperature, heat transfer coefficient, and pressure drop are used as outcomes to evaluate these parameters.

Table 6. Parameters and Outcomes.

Variables	Outcome
• Re = 890 to 1500 based on Qu and Mudawar [33] • Nanoparticles volume fraction (1.0 to 7.0 % for Al_2O_3–H_2O, SiO_2–H_2O, and TiO_2–H_2O) • Geometry (single stack rectangle, trapezoid, triangle, and circle)	T: MCHS temperature h: Heat transfer coefficient Δp: Pressure drop

2.5. Boundary Conditions

Firstly, different nanoparticle types (Al_2O_3, SiO_2, and TiO_2) are investigated for different concentrations to explore the best type of nanoparticle and the optimum concentration that fulfills a good balance between the desired heat transfer and power consumption. Secondly, according to the first study, different microchannel configurations (rectangular, trapezoidal, triangular, and circular), indicated in Figures 1–4, are studied using the best type of nanoparticle found in the first study. The laminar fluid flow in the current study is used using Reynolds numbers ranging from 890 to 1500, which leads to different values for the inlet velocity boundary condition at x = 0. The inlet velocity can be calculated using Equation (13) and indicated in Tables 7–12 for all nanoparticle types and configurations. The fluid flow is considered fully developed at both outlet and inlet. The heat source with constant heat flux at the bottom of the channel was calculated at q= 10^6 W/m^2, and the inlet temperature was seized as T_{in} = 288 K.

$$u_{in} = \frac{Re\mu}{\rho D_h}, \quad (13)$$

where the Reynolds number is Re, the fluid density is ρ, the hydraulic diameter is D_h, and the dynamic viscosity is μ.

Table 7. Inlet velocity for a rectangular MCHS using Al_2O_3–water.

Re	φ = 0	0.01	0.03	0.05	0.06	0.07	T_{in} (k)	q (W/m^2)
	u_{in} (m/s)							
890	2.187	2.177	2.158	2.141	2.134	2.126		
1000	2.458	2.446	2.425	2.406	2.397	2.389		
1100	2.703	2.691	2.667	2.647	2.637	2.628	288	10^6
1300	3.195	3.180	3.151	3.128	3.117	3.106		
1500	3.686	3.670	3.637	3.609	3.596	3.584		

Table 8. Inlet velocity for a rectangular MCHS using TiO_2–water.

Re	φ = 0	0.01	0.03	0.05	0.06	0.07	T_{in} (k)	q (W/m^2)
	u_{in} (m/s)							
890	2.187	2.173	2.147	2.124	2.113	2.103		
1000	2.458	2.442	2.413	2.387	2.375	2.363		
1100	2.703	2.686	2.654	2.625	2.612	2.600	288	10^6
1300	3.195	3.174	3.136	3.103	3.087	3.072		
1500	3.686	3.662	3.619	3.580	3.562	3.545		

Table 9. Inlet velocity for a rectangular MCHS using SiO_2–water.

Re	φ = 0	0.01	0.03	0.05	0.06	0.07	T_{in} (k)	q (W/m^2)
	u_{in} (m/s)							
890	2.187	2.215	2.269	2.321	2.346	2.370		
1000	2.458	2.489	2.550	2.607	2.635	2.663		
1100	2.703	2.738	2.805	2.868	2.899	2.929	288	10^6
1300	3.195	3.236	3.315	3.390	3.426	3.462		
1500	3.686	3.734	3.824	3.911	3.953	3.994		

Table 10. Inlet velocity for a trapezoidal MCHS using Al_2O_3–water.

Re	φ = 0	0.01	0.03	0.05	0.06	0.07	T_{in} (k)	q (W/m^2)
	u_{in} (m/s)							
890	2.608	2.595	2.573	2.553	2.544	2.535	288	10^6
1000	2.930	2.916	2.891	2.868	2.858	2.848		
1100	3.223	3.208	3.180	3.155	3.144	3.133		
1300	3.809	3.791	3.758	3.729	3.715	3.703		
1500	4.395	4.374	4.337	4.303	4.287	4.272		

Table 11. Inlet velocity for a Triangular MCHS using Al_2O_3–water.

Re	φ = 0	0.01	0.03	0.05	0.06	0.07	T_{in} (k)	q (W/m^2)
	u_{in} (m/s)							
890	3.583	3.566	3.535	3.507	3.495	3.483	288	10^6
1000	4.025	4.006	3.972	3.941	3.927	3.913		
1100	4.428	4.407	4.369	4.335	4.319	4.304		
1300	5.233	5.208	5.163	5.123	5.105	5.087		
1500	6.038	6.010	5.958	5.911	5.890	5.869		

Table 12. Inlet velocity for a Circular MCHS using Al_2O_3–water.

Re	φ = 0	0.01	0.03	0.05	0.06	0.07	T_{in} (k)	q (W/m^2)
	u_{in} (m/s)							
890	1.667	1.659	1.645	1.632	1.626	1.620	288	10^6
1000	1.873	1.864	1.848	1.833	1.827	1.820		
1100	2.060	2.050	2.033	2.017	2.009	2.002		
1300	2.434	2.423	2.402	2.383	2.375	2.367		
1500	2.809	2.796	2.772	2.750	2.740	2.731		

3. Results and Discussion

The coolant temperature along the centerline is used as a key parameter to investigate the mesh sensitivity. Three different mesh levels (Mesh 1, Mesh 2, and Mesh 3) of cell volumes (20, 40, and 60 μm^3, respectively) are used. Pure water at constant heat flux, q = 10^6 W/m^2, and Re = 890 are applied in this study. Figure 5 indicates that the predicted center line temperature is mesh-independent. The figure indicates that the centerline temperature results are very close for all meshes, with the differences in local temperature being less than 0.5%. Additionally, due to small differences in the run time for all cases, all reported subsequent results have been obtained using the smallest cell volume (Mesh 1) to increase the accuracy and resolution of the results. On the other hand, the experimental data obtained by Qu and Mudawar [33] and Arulprakasajothi et al. [34] are used to examine the current numerical results' validity for pure water [33] and TiO_2/water nanofluids [34]. The heatsink temperature distribution along the line that is parallel to the microchannel centerline is used for validity purposes using Qu and Mudawar's data. While Nusselt number variation with Reynolds number is used for verification purposes using Arulprakasajothi et al.'s data [34]. In the validation study, the model is a rectangular MCHS configuration with channel height, width, hydraulic diameter, and length of 713 μm, 231 μm, 348.9 μm, and 44.764 mm, respectively. The experimental data [33] for a temperature measured by thermocouples along an x-y plane and four different locations at the height of 3175 μm, shown in Figure 6a, are obtained at a constant heat flux of q = 10^6 W/m^2, T_{in} = 288 k, and Re = 890. Figure 6 indicates an acceptable agreement between the CFD (current work) and the experimental data [33,34]. Thus, the current model is trusted and can be applied to investigate different nanofluids as a coolant and different microchannel configurations and their effects on the flow and heat transfer characteristics of an MCHS.

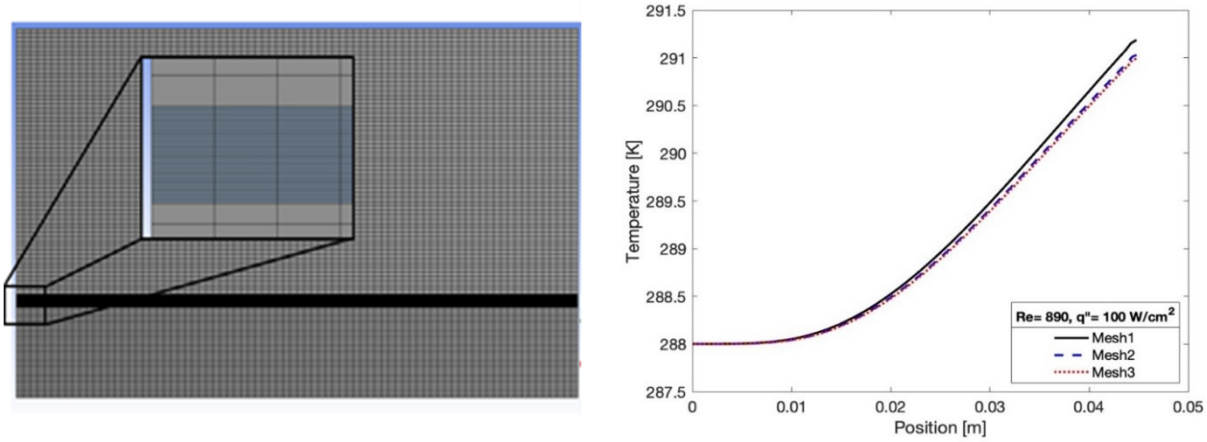

Figure 5. (**a**) Grid layout and (**b**) mesh sensitivity study.

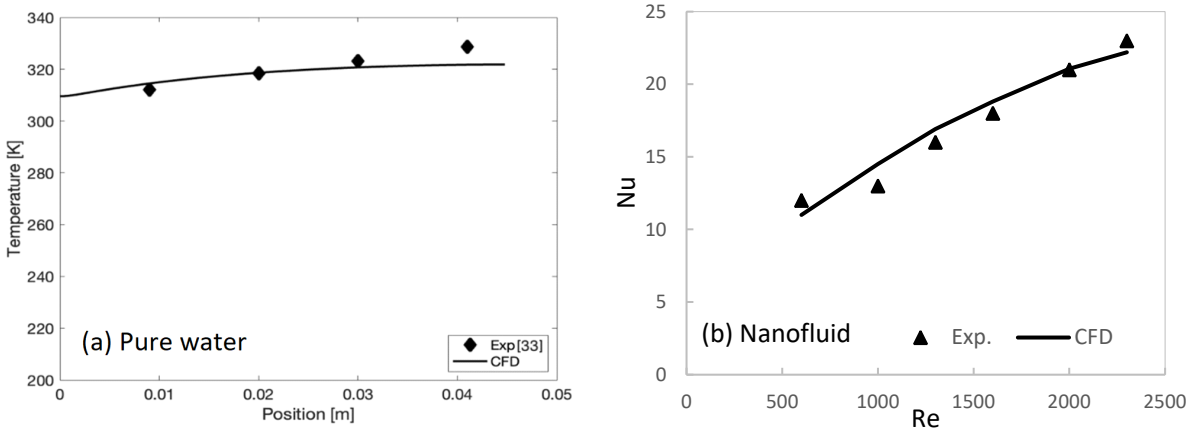

Figure 6. CFD validation with experimental data using (**a**) pure water and (**b**) nanofluid.

3.1. Different Nanofluid

Various nanofluids, such as Al_2O_3–H_2O, SiO_2–H_2O, and TiO_2–H_2O, are investigated using rectangular MCHS. The volume concentration of different nanoparticles ranging from 1% to 7% at Reynolds numbers ranging from 890 to 1500 is studied. Figure 7 shows the effect of Re on the heat transfer coefficient for different concentrations of Al_2O_3 nanoparticles. The heat transfer coefficient (represented values are in 10 thousand) for all concentrations increased with increasing Reynolds number and was significantly higher than the pure water. The results showed that the larger percentage of Al_2O_3 nanoparticles contributes to the higher heat transfer coefficient. For example, at Re = 1500 and $\varphi = 7\%$, the heat transfer coefficient reached the highest value with an increment of 8.58% compared to pure water. In Figure 8, the effect of both Re and φ on the average heat transfer coefficient "h" is more conventionally shown by plotting the normalized heat transfer coefficient that is a non-dimensional quantity, $\frac{h - h_w}{h_w}$, with Re, where h and h_w represent the average heat transfer coefficient of both nanofluid and base fluid (water), respectively. The normalized heat transfer coefficient significantly increased with nanofluid concentration and was nearly constant with Re numbers. As observed, a greater normalized heat transfer coefficient improvement is achieved at the higher concentration. For instance, at Re = 890 and $\varphi = 7\%$, a 9.89% increase in heat transfer coefficient improvement was indicated. This means that adding more nanoparticles leads to a better cooling process.

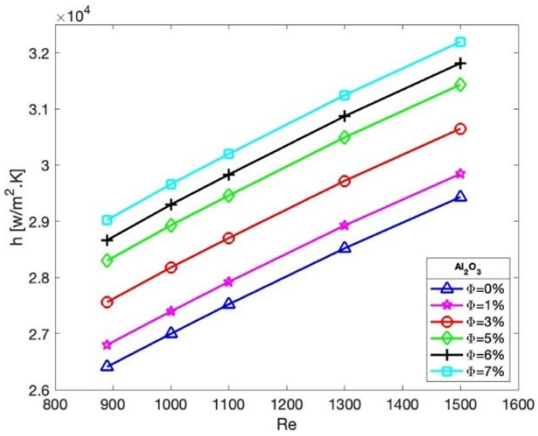

Figure 7. Effect of Re on the average heat transfer coefficient for rectangular MCHS at different Al_2O_3 concentrations.

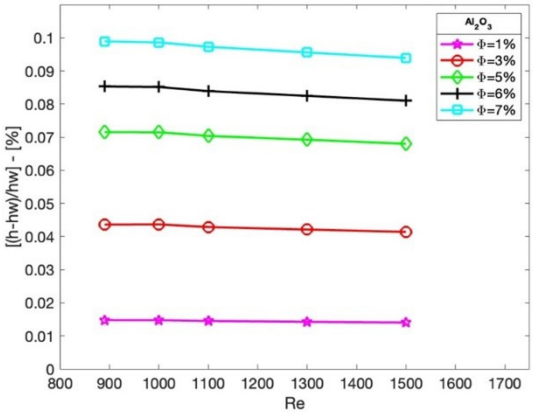

Figure 8. Effect of Re on normalized average heat transfer coefficient for rectangular MCHS at different Al_2O_3.

The pressure drop profile for different concentrations of Al_2O_3 nanoparticles is shown in Figure 9. From this figure, the relation between pressure drop and Reynolds number at different concentrations can be observed. The figure indicates that the pressure drop rises linearly with the Reynolds number. It is also observed that the pressure drop increases with increasing nanoparticle concentration. For example, the maximum pressure drop occurred at $\varphi = 7\%$ and Re = 1500. The percentage of pressure drop increment at $\varphi = 7\%$ compared with pure water is 12.4%. This increment is due to the increase of nanofluid dynamic viscosity compared with the corresponding value for pure water.

A comparison between different nanofluids is drawn for Al_2O_3–H_2O, SiO_2–H_2O, and TiO_2–H_2O at different Re numbers and nanoparticle concentrations. Figure 10a,b shows the heat transfer coefficient variation of Al_2O_3–H_2O, SiO_2–H_2O, and TiO_2–H_2O at different Re for $\varphi = 1\%$ and $\varphi = 7\%$. It can be inferred that all nanoparticles have the same linear increasing trend with Re. Comparing the heat transfer coefficient of pure water at Re = 890 and nanofluids at $\varphi = 1\%$, it was found that the heat transfer coefficients for Al_2O_3, TiO_2, and SiO_2 increased by 1.48%, 1.33%, and 0.81%, respectively. While the corresponding heat transfer coefficient increment at Re = 890 and $\varphi = 7\%$, shown in Figure 10b, are 9.82%, 8.87%, and 5.04% for Al_2O_3, TiO_2, and SiO_2, respectively. As a result, the maximum heat transfer coefficient is obtained by Al_2O_3–H_2O at all concentrations.

Figure 11a,b shows the relationship between the pressure drop and Re for the three different nanofluids mentioned above, at $\varphi = 1\%$ and $\varphi = 7\%$, respectively. It is found that by increasing the Reynolds number, the pressure drop increases with the maximum pressure drop for SiO_2 compared with pure water. Additionally, both figures indicate that

there is a slight difference between the pressure drop for both Al_2O_3 and TiO_2. In more detail, the increment of pressure drops for SiO_2, TiO_2, and Al_2O_3 are estimated to be 3.67%, 1.84%, and 2.02% compared with pure water, respectively. The corresponding increments of pressure drop at $\varphi = 7\%$, shown in Figure 11b, are 21.45%, 14.22%, and 12.99% for SiO_2, Al_2O_3, and TiO_2, respectively. As a result, an increase in the concentration of nanoparticles leads to an increase in the viscosity of the nanofluids as well as the friction factor and pressure drop.

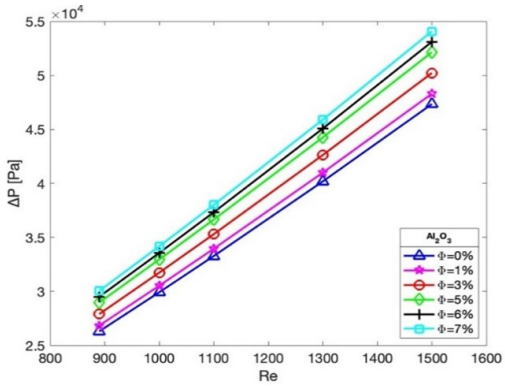

Figure 9. Pressure drop variation at different Re and different Al_2O_3 concentrations for rectangular MCHS.

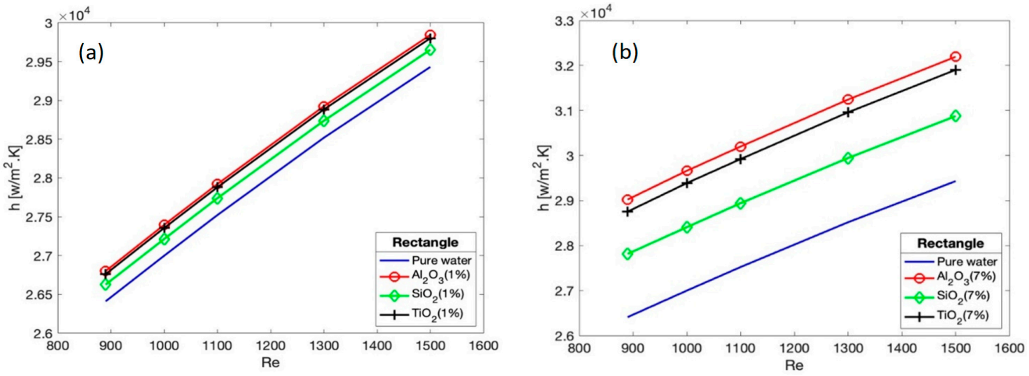

Figure 10. Average heat transfer coefficient for Al_2O_3–H_2O, SiO_2–H_2O, and TiO_2–H_2O at (**a**) φ = 1% and (**b**) φ = 7%.

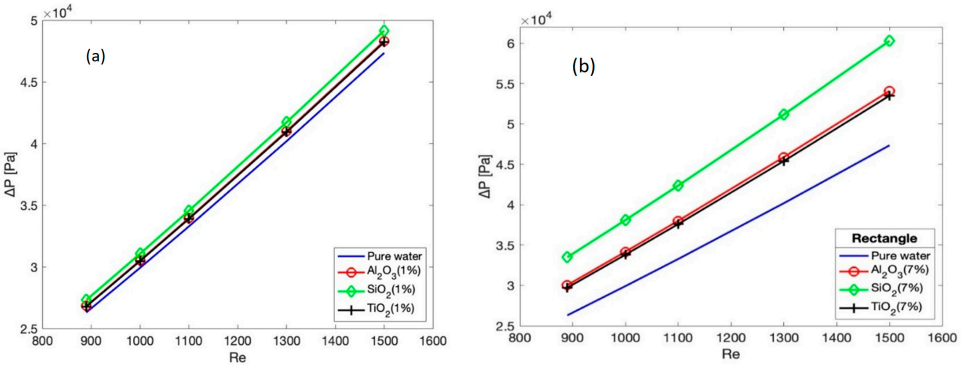

Figure 11. Pressure drop increasing with Re for Al_2O_3–H_2O, SiO_2–H_2O, and TiO_2–H_2O at (**a**) φ = 1% and (**b**) φ = 7%.

3.2. Different MCHS Configurations

As discussed in Section 3.1, the Al_2O_3–H_2O achieves the highest average heat transfer coefficient; therefore, this type of nanofluid is used to investigate the different configurations

of MCHS, shown in Figures 1–4. The average heat transfer coefficient, pressure drop, and thermal efficiency are used as key parameters to evaluate the suitable configuration that achieves the best heat transfer rate. Figure 12 represents the effect of both Re and different MCHS configurations (rectangular, trapezoidal, triangular, and circular) on the average heat transfer for (a) φ = 1% and (b) φ = 7%. The pure water (φ = 0%) results are shown in Figure 12 as solid lines for clear comparison and evaluation. The heat transfer coefficient for all geometrical configurations increases with both Re and φ. According to the figure, the maximum and minimum heat transfer coefficients are obtained for triangular and circular configurations, respectively, while the trapezoidal and rectangular are sandwiched between triangular and circular geometry. For example, at Re = 890 and φ = 7%, the heat transfer coefficient increments of triangular, rectangular, trapezoidal, and circular increases by 7.473%, 9.889%, 8.941%, and 10.951% compared with pure water of the same configurations, respectively. As a result, different MCHS configurations significantly affected the heat transfer properties. The triangular configuration is considered the best configuration that results in the greatest heat transfer coefficient.

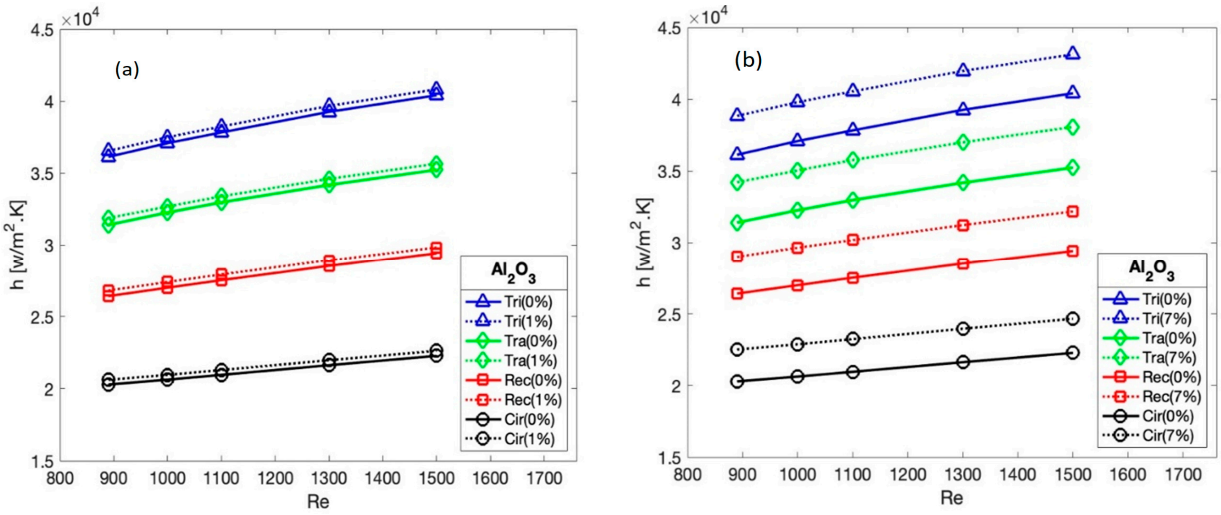

Figure 12. Average heat transfer coefficient for rectangular, trapezoidal, triangular, and circular MCHS using Al_2O_3 at (**a**) φ = 1% and (**b**) φ = 7%.

Figure 13 shows the variation of pressure drop across the MCHS for different configurations and different Reynolds numbers at (a) φ = 1% and (b) φ = 7%. It is clearly shown that the pressure drop rises with both Re and φ. Triangular MCHS causes the highest pressure drop compared to the other configurations. The pure water flows through the rectangular MCHS and is used as a reference value to evaluate the other configurations and nanofluids. For example, at Re = 890 and φ = 1%, the pressure drop increase of the triangular domain was 2.3 times more than that of pure water in the rectangular MCHS. On the contrary, the circular domain at Re = 890 showed an increase of 0.52 times more than that of the same reference. While at φ = 7%, indicated in Figure 13b, the pressure drops of triangular and circular MCHS increased by 2.72 and 0.46 times compared with the pure water of the rectangular MCHS, respectively. The reason for the above results can be due to the hydraulic diameter, where the hydraulic diameter (Equation (12)) of a triangular shape is smaller than the circular one.

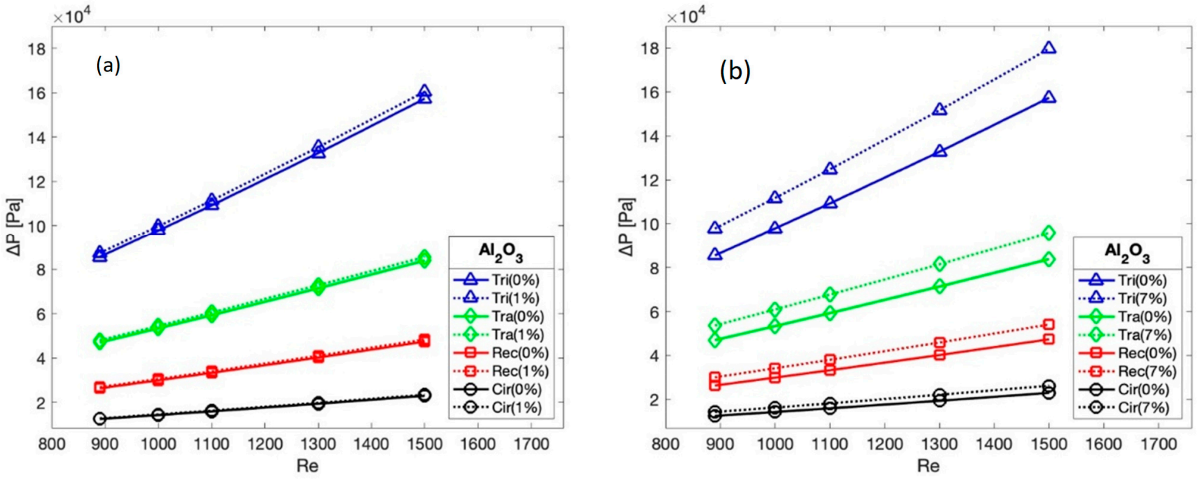

Figure 13. Pressure drop increase with Re for rectangular, trapezoidal, triangular, and circular MCHS using Al_2O_3 at (**a**) φ = 1% and (**b**) φ = 7%.

In order to give a clear understanding of the effect of different configurations of MCHS on the heat transfer and flow characteristics, the thermal efficiency (Equation (14)), which is the ratio between the heat transfer rate and the power consumption, is introduced as follows:

$$\eta_{th} = \frac{\text{Heat transfer rate}}{\text{power}} = \frac{\rho c_p (T_{out} - T_{in})}{\Delta p}. \quad (14)$$

Figure 14 shows the thermal efficiency of all configurations. As shown in the figure, the maximum and minimum thermal efficiency are achieved by the circular and triangular MCHS, respectively. However, triangular MCHS leads to the maximum heat transfer coefficient, but at the same time, it has a maximum hydraulic diameter that leads to a high-pressure drop. According to these results, it is very important to understand that nanofluids have advantages related to heat transfer and disadvantages related to power consumption. In summary, the higher the volume of nanoparticle concentration, the higher the heat transfer coefficient and the higher the pressure drop.

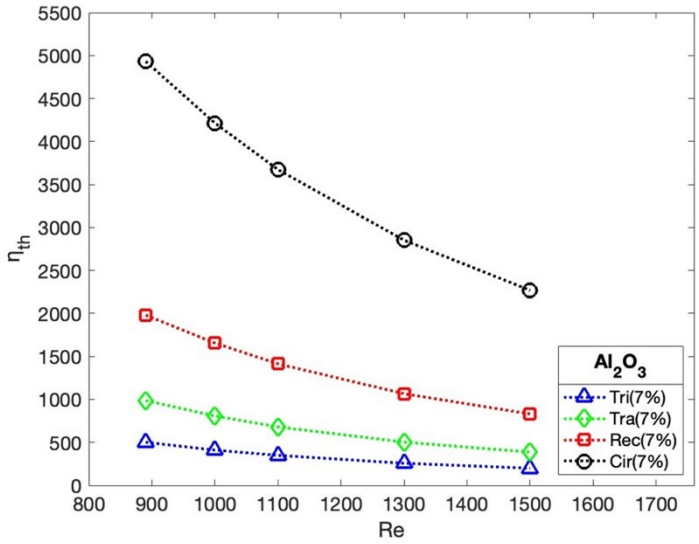

Figure 14. Thermal efficiency in triangular, trapezoidal, rectangular, and circular MCHS at φ = 7.

4. Conclusions

In the present study, 3-D fluid laminar flow and heat transfer in the microchannel are computationally studied. Different nanoparticles (Al_2O_3, SiO_2, and TiO_2) and different

MCHS configurations (rectangular, trapezoidal, triangular, and circular) are investigated. Based on the simulation results, the following conclusions can be drawn:

- For all values of nanoparticle volume fractions, the temperature of both the coolant fluid and MCHS increases along the channel axis;
- Increasing the concentration of nanoparticles leads to an increase in the average heat transfer coefficient and significantly reduces the temperature of the MCHS compared with that of pure water;
- The maximum average heat transfer coefficient is achieved by using the Al_2O_3 at φ = 7% with an increment of 8.58% compared with the pure water. While the minimum values are fulfilled by using SiO_2, and the values for TiO_2 are sandwiched in between;
- SiO_2 at low and high concentrations of nanoparticles causes the highest pressure drop compared with the corresponding values for Al_2O_3 and TiO_2 at all values of Re;
- The study of MCHS with different configurations shows that the triangular MCHS leads to the greatest heat transfer coefficient as well as pressure drop compared with the other configurations (trapezoidal, rectangular, and circular) having the same cross-sectional area, same Re, same nanoparticles, and same heat flux.

Author Contributions: Conceptualization, I.E., M.F., A.D., M.A., I.M. and W.A.-K.; methodology, I.E.; software, I.E., A.A., M.D., Y.A. and W.A.-K.; validation, A.A., M.D. and Y.A.; formal analysis, I.E., and W.A.-K.; investigation, I.E.; resources, I.E.; data curation, I.E.; writing—original draft preparation, A.A., M.D. and Y.A.; writing—review and editing, I.E., M.F., A.D., M.A., I.M. and W.A.-K.; visualization, I.E.; supervision, I.E.; project administration, I.E.; funding acquisition, I.E. All authors have read and agreed to the published version of the manuscript.

Funding: This research received no external funding.

Data Availability Statement: The datasets generated during the current study are available from the corresponding author on reasonable request.

Conflicts of Interest: The authors declare no conflict of interest.

Nomenclature

A	Area (m^2)
C_p	Specific heat capacity (J/kg·k)
D_h	Hydraulic diameter (m)
H	Height or thickness (m)
h	Heat transfer coefficient (W/m·K)
Nu	Nusselt number
q	Heat flux (W/m^2)
Re	Reynolds number
u	Inlet velocity (m/s)
x, y, z	Cartesian coordinates
T	Temperature (K)
W	Width (m)
k	Thermal conductivity (W/m·K)
L	Channel length (m)
Greek Symbols	
ρ	Fluid density (kg/m^3)
μ	Dynamic viscosity (kg/m·s)
φ	Particle volume fraction

Subscript	
av	Average
f	Fluid
nf	Nanofluid
p	Solid particles
b	Bulk
ch	Channel
in	Inlet
out	Outlet
th	Thermocouple location
t	Top thickness

References

1. Tuckerman, D.B.; Pease, R.F.W. High-performance heat sinking for VLSI. *IEEE Electron Device Lett.* **1981**, *2*, 126–129. [CrossRef]
2. Chen, Y.; Zhang, C.; Shi, M.; Wu, J. Three-dimensional Numerical Simulation of Heat and Fluid Flow in Noncircular Microchannel Heat Sin. *Int. Commun. Heat Mass Transf.* **2009**, *36*, 917–920. [CrossRef]
3. Gunnasegaran, P.; Mohamed, H.A.; Shuaib, N.H.; Saidur, R. The Effect of Geometrical Parameters on Heat Transfer Characteristics of Microchannels Heat Sink with Different Shapes. *Int. Commun. Heat Mass Transf.* **2010**, *37*, 1078–1086. [CrossRef]
4. Ahmed, H.E.; Ahmed, M.I. Optimum Thermal Design of Triangular, Trapezoidal and Rectangular Grooved Microchannel Heat Sinks. *Int. Commun. Heat Mass Transf.* **2015**, *66*, 47–57. [CrossRef]
5. Trisaksri, V.; Wongwises, S. Critical Review of Heat Transfer Characteristics of Nanofluid. *Renew. Sustain. Energy Rev.* **2007**, *11*, 512–523. [CrossRef]
6. Choi, S.U.S.; Eastman, J.A. Enhancing thermal conductivity of fluids with nanoparticles. In Proceedings of the 1995 International Mechanical Engineering Congress and Exhibition, San Francisco, CA, USA, 12–17 November 1995; ASME: New York, NY, USA, 1995; pp. 99–105.
7. Godson, L.; Raja, B.; Lal, D.M.; Wongwises, S. Enhancement of heat transfer using nanofluids. An overview. *Renew. Sustain. Energy Rev.* **2010**, *14*, 629–641. [CrossRef]
8. Mat Tokit, E.; Yusoff, M.Z.; Mohammed, H.A. Generality of Brownian motion velocity of two phase approach in interrupted microchannel heat sink. *Int. Commun. Heat Mass Transf.* **2013**, *49*, 128–135. [CrossRef]
9. Das, S.K.; Putra, N.; Thiesen, P.; Roetzel, W. Temperature dependence of thermal conductivity enhancement for nanofluids. *J. Heat Transf.* **2003**, *125*, 567–574. [CrossRef]
10. Salman, B.H.; Mohammed, H.A.; Kherbeet, A.S. Heat transfer enhancement of nanofluids flow in microtube with constant heat flux. *Int. Commun. Heat Mass Transf.* **2012**, *39*, 1195–1204. [CrossRef]
11. Nguyen, C.T.; Roy, G.; Gauthier, C.; Galanis, N. Heat transfer enhancement using Al_2O_3–water nanofluid for an electronic liquid cooling system. *Appl. Therm. Eng.* **2007**, *27*, 1501–1506. [CrossRef]
12. Elbadawy, I.; Fayed, M. Reliability of Al_2O_3 Nanofluid Concentration on the Heat Transfer Augmentation and Resizing for Single and Double Stack Microchannels. *Alex. Eng. J.* **2020**, *59*, 1771–1785. [CrossRef]
13. Mohammed, H.A.; Gunnasegaran, P.; Shuaib, N.H. The impact of various nanofluid types on triangular microchannels heat sink cooling performance. *Int. Commun. Heat Mass Transf.* **2011**, *39*, 767–773. [CrossRef]
14. Al-Kouz, W.; Bendrer, B.A.-I.; Aissa, A.; Almuhtady, A.; Jamshed, W.; Nisar, K.S.; Mourad, A.; Alshehri, N.A.; Zakarya, M. Galerkin finite element analysis of magneto two-phase nanofluid flowing in double wavy enclosure comprehending an adiabatic rotating cylinder. *Sci. Rep.* **2021**, *11*, 16494. [CrossRef]
15. Al-Farhany, K.; Al-dawody, M.F.; Hamzah, D.A.; Al-Kouz, W.; Said, Z. Numerical investigation of natural convection on Al_2O_3−water porous enclosure partially heated with two fins attached to its hot wall: Under the MHD effects. *Appl. Nanosci.* **2021**, *13*, 555–572. [CrossRef]
16. Sohail, M.; Nazir, U.; Chu, Y.M.; Al-Kouz, W.; Thounthong, P. Bioconvection phenomenon for the boundary layer flow of magnetohydrodynamic Carreau liquid over a heated disk. *Sci. Iran.* **2021**, *28*, 1896–1907.
17. Al-Kouz, W.; Abderrahmane, A.; Shamshuddin, M.D.; Younis, O.; Mohammed, S.; Bég, O.A.; Toghraie, D. Heat transfer and entropy generation analysis of water-Fe_3O_4/CNT hybrid magnetic nanofluid flow in a trapezoidal wavy enclosure containing porous media with the Galerkin finite element method. *Eur. Phys. J. Plus* **2021**, *136*, 1184. [CrossRef]
18. Rana, P.; Al-Kouz, W.; Mahanthesh, B.; Mackolil, J. Heat transfer of TiO_2 − EG nanoliquid with active and passive control of nanoparticles subject to nonlinear Boussinesq approximation. *Int. Commun. Heat Mass Transf.* **2021**, *126*, 105443. [CrossRef]
19. Al-Kouz, W.; Medebber, M.A.; Elkotb, M.A.; Abderrahmane, A.; Aimad, K.; Al-Farhany, K.; Jamshed, W.; Moria, H.; Aldawi, F.; Saleel, C.A.; et al. Galerkin finite element analysis of Darcy–Brinkman–Forchheimer natural convective flow in conical annular enclosure with discrete heat sources. *Energy Rep.* **2021**, *7*, 6172–6181. [CrossRef]
20. Mahesh, A.; Varma SV, K.; Raju CS, K.; Babu, M.J.; Vajravelu, K.; Al-Kouz, W. Significance of non-Fourier heat flux and radiation on PEG–water based hybrid nanofluid flow among revolving disks with chemical reaction and entropy generation optimization. *Int. Commun. Heat Mass Transf.* **2021**, *127*, 105572. [CrossRef]

21. Al-Kouz, W.; Al-Waked, R.; Sari, M.E.; Owhaib, W.; Atieh, A. Numerical study of heat transfer enhancement in the entrance region for low-pressure gaseous laminar pipe flows using Al_2O_3–air nanofluid. *Adv. Mech. Eng.* **2018**, *10*, 1687814018784410. [CrossRef]
22. Ferhi, M.; Djebali, R.; Al-Kouz, W.; Abboudi, S.; Chamkha, A.J. MHD conjugate heat transfer and entropy generation analysis of MWCNT/water nanofluid in a partially heated divided medium. *Heat Transf.* **2021**, *50*, 126–144. [CrossRef]
23. Rana, P.; Mahanthesh, B.; Mackolil, J.; Al-Kouz, W. Nanofluid flow past a vertical plate with nanoparticle aggregation kinematics, thermal slip and significant buoyancy force effects using modified Buongiorno model. *Waves Random Complex Media* **2021**. [CrossRef]
24. Elbadawy, I.; Elsebay, M.; Shedid, M.; Fatouh, M. Reliability of Nanofluid Concentration on the Heat Transfer Augmentation in Engine Radiator. *Int. J. Automot. Technol.* **2018**, *19*, 233–243. [CrossRef]
25. *ANSYS FLUENT 14.0 User Guide*; ANSYS, Inc., Southpointe: Canonsburg, PA, USA, 2011.
26. Elbadawy, I.; Anbr, S.; Fatouh, M. Heat transfer Characteristics of Water Flowing through Single and Double Stack Rectangular Microchanels. In Proceedings of the 16th Int. AMME Conference, Cairo, Egypt, 27–29 May 2014.
27. Patankar, S. *Numerical Heat Transfer and Fluid Flow*; Hemisphere: New York, NY, USA, 1980.
28. Tao, W.Q. *Numerical Heat Transfer*, 2nd ed.; Xi'an Jiaotong University Press: Xi'an, China, 2001.
29. Xie, X.L.; Liu, Z.J.; He, Y.L.; Tao, W.Q. Numerical study of laminar heat transfer and pressure drop characteristics in a water-cooled minichannel heat sink. *Appl. Therm. Eng.* **2009**, *29*, 64–74. [CrossRef]
30. Jaeseon, L.; Mudawar, I. Assessment of the effectiveness of nanofluids for single-phase and two-phase heat transfer in micro-channels. *Int. J. Heat Mass Transf.* **2007**, *50*, 452–463.
31. Hung, T.-C.; Yan, W.-M.; Wang, X.-D.; Chang, C.-Y. Heat transfer enhancement in microchannel heat sinks using nanofluids. *Int. J. Heat Mass Transf.* **2012**, *55*, 2559–2570. [CrossRef]
32. Ferrouillat, S.; Bontemps, A.; Ribeiro, J.P.; Gruss, J.A.; Soriano, O. Hydraulic and heat transfer study of SIO_2/water nanofluids in horizontal tubes with imposed wall temperature boundary conditions. *Int. J. Heat Fluid Flow* **2011**, *32*, 424–439. [CrossRef]
33. Qu, W.; Mudawar, I. Experimental and numerical study of pressure drop and heat transfer in a single-phase micro-channel heat sink. *Int. J. Heat Mass Transf.* **2002**, *45*, 2549–2565. [CrossRef]
34. Arulprakasajothi, M.; Elangovan, K.; Reddy, K.H.; Suresh, S. Heat transfer study of water-based Nanofluids containing titanium oxide nanoparticle. In Proceedings of the 4th International Conference on Materials Processing and Characterization, Hyderabad, India, 14–15 February 2015; pp. 3648–3655.